

---

# LEVERAGING CONVOLUTIONAL AND GRAPH NETWORKS FOR AN UNSUPERVISED REMOTE SENSING LABELLING TOOL

---

**Tulsi Patel** 

Department of Computer Science  
Swansea University  
Swansea  
912100@swansea.ac.uk

**Mark W. Jones** 

Department of Computer Science  
Swansea University  
Swansea  
M.W.Jones@swansea.ac.uk

**Thomas Redfern**

UK Hydrographic Office  
Taunton TA1 2DN, UK  
Thomas.Redfern@UKHO.gov.uk

August 1, 2025

## ABSTRACT

Machine learning for remote sensing imaging relies on up-to-date and accurate labels for model training and testing. Labelling remote sensing imagery is time and cost intensive, requiring expert analysis. Previous labelling tools rely on pre-labelled data for training in order to label new unseen data. In this work, we define an unsupervised pipeline for finding and labelling geographical areas of similar context and content within Sentinel-2 satellite imagery. Our approach removes limitations of previous methods by utilising segmentation with convolutional and graph neural networks to encode a more robust feature space for image comparison. Unlike previous approaches we segment the image into homogeneous regions of pixels that are grouped based on colour and spatial similarity. Graph neural networks are used to aggregate information about the surrounding segments enabling the feature representation to encode the local neighbourhood whilst preserving its own local information. This reduces outliers in the labelling tool, allows users to label at a granular level, and allows a rotationally invariant semantic relationship at the image level to be formed within the encoding space.

**Keywords** Satellite Imagery, Remote Sensing, Graph Neural Networks, Unsupervised Clustering, Interactive Labelling Tool, Fuzzy C-Means, Dimension Reduction, UMAP

## 1 Introduction

Rapid advancements in satellite imagery and Remote Sensing (RS) have led to an explosion of data, with the Sentinel-2 mission producing 1.6 terabytes of data daily. This wealth of data enables applications across agriculture, land use mapping, environmental monitoring, coastal management and monitoring and geological studies [Karthikeyan et al., 2020, Zhang and Zhang, 2022, Weiss et al., 2020, Ahmadi and Pekkan, 2021, Seale et al., 2022] – all of which require high quality labelled datasets. The relatively large pixel resolutions of Sentinel-2 (covering 10 to 60m) create challenges for labelling. A single pixel, representing a 10m by 10m area, might cover both land and water, leading to significant variation in the quantities of each within the same pixel. Dataset labels can consist of small image segments that have a feature of interest present, labelled bounding boxes or pixel level labels.

There is a pressing need for accurate labelled datasets in remote sensing to enable reliable analysis and model training. A notable gap in remote sensing tools for labelling was identified by Li et al. [Li et al., 2021a], who developed LabelRS – a segmentation and dataset-building tool. LabelRS leverages open-source data from OpenStreetMaps, Land Use Land Cover (LULC) datasets, and ArcGIS user annotations. While it is effective for generating semantic, object, or image classification datasets, its reliance on predefined label categories limits flexibility, making it less adaptable to new or unseen categories.

To address this challenge, we sought to develop a toolchain that enhances labelling efficiency by presenting experts with similar content for quick and accurate annotation. We turned to the related field of Content-Based Image Retrieval (CBIR), which aims to retrieve similar content through three main steps: 1) feature representation, 2) indexing, and 3) similarity measurement [Li et al., 2021b]. By leveraging CBIR’s ability to present relevant images in an unsupervised context, we can offer increased flexibility and time efficiency, assuming the retrieved content is sufficiently similar. Several image retrieval tools have adopted CBIR to return a list of images most similar to a target query, such as those described in [Qi et al., 2020, Hou et al., 2019].

CBIR methods typically begin with low-level feature extractors that focus on local texture, colour (spectral), and shape characteristics. Examples of such feature extraction techniques include the Scale-Invariant Feature Transform (SIFT) [Chen et al., 2020, Zhu et al., 2016], Gray-Level Co-occurrence Matrices (GLCM), wavelets, Gabor filters, and Local Binary Patterns (LBP) [Huang et al., 2014, Ranchin and Wald, 1993, Yang and Newsam, 2008, Huang et al., 2016]. These techniques primarily focus on either texture features (which capture spectral relationships) or the spectra themselves. Once extracted, these low-level features can be further processed into mid-level representations using algorithms like the Vector of Locally Aggregated Descriptors (VLAD), Bag of Visual Words (BoW), or Bag of Features [Jégou et al., 2010, Sivic and Zisserman, 2003, Cao et al., 2010]. BoW is a foundational technique that employs K-means clustering to create a visual codebook, which then generates histograms of local features. While widely used, BoW is often outperformed by VLAD, which improves upon it by capturing the spatial relationships between local features and their corresponding cluster centres.

Deep Convolutional Neural Networks (DCNNs) [Song et al., 2019] can replace traditional low-level feature extractors, leading to substantial improvements in image retrieval performance [Imbriaco et al., 2019, Bosilj et al., 2016]. For instance, Wang et al. [Wang et al., 2017] employ multiple convolutional layers to build hierarchical feature sets, which are then enhanced using VLAD descriptors. Their work demonstrates the efficacy of DCNN architectures such as VGG, ResNet, OverFeat, and CaffeNet in this context. More advanced models like NetVLAD and SatResNet-50 outperform

traditional hand-crafted descriptors in terms of retrieval accuracy [Napoletano, 2018]. Additionally, these DCNN-based methods can function in an unsupervised manner, utilising techniques like autoencoders, generative models, and a combination of support vector machines (SVMs) or visual codebooks [Romero et al., 2015, Tang et al., 2018, Sun and Bourennane, 2020]. Wang et al. [Wang et al., 2021] propose a deep hashing approach using Graph Neural Networks (GNNs), where deep features are extracted from a pre-trained ResNet network.

Despite their effectiveness, a limitation of visual codebook-based methods is that they often lose semantic relationships between image features. To overcome this, Sumbul and Demir [Sumbul and Demir, 2021] explore multi-label co-occurrence relationships in remote sensing (RS) images. They employ a CNN feature extractor, which feeds into a Graph Neural Network (GNN) that compares features using multiple Siamese Neural Networks (SNN), each with a different form of triplet loss to refine the results. Yu et al. [Yu et al., 2022] leverage GNNs for cross-model text-image matching, showing significant improvements when combined with attention mechanisms. Similarly, Kang et al. [Kang et al., 2021] enhance multi-label image retrieval by using graph structures to better represent the relationships between multiple semantic annotations.

By better organising the feature space, these methods can improve matching accuracy. Explicit feature space manipulation techniques, such as triplet loss [Zhang et al., 2021, Yan et al., 2020, Draganov and Dohn, 2023], have shown promise in this area. Halladin-Dąbrowska et al. [Halladin-Dąbrowska et al., 2019] used t-SNE to enhance reference data for heterogeneous non-forest vegetation. Their approach, which employs unsupervised dimensionality reduction, differs from previous methods by eliminating the need for predefined label categories – an issue in many remote sensing applications where label definitions vary widely. Additionally, their method provides contextual feedback about the relationships between features, such as distinguishing urban areas from surrounding land or dense urban zones. This contextual discrimination, based on geographical proximity, allows labellers to customise datasets more effectively, ensuring they can balance and fine-tune their labelled datasets according to specific requirements.

Our research addresses the gap between low-level features and high-level semantic concepts, as identified by Chaudhuri et al. [Chaudhuri et al., 2018]. They proposed a sub-graph matching strategy that emphasizes neighbourhood contexts within segmented images. While effective, this approach is computationally expensive [Chaudhuri et al., 2018]. More recent work [Chaudhuri et al., 2022] improves on this by using contrastive loss between Siamese Graph Convolutional Networks (GCNs), replacing sub-graph matching. This method applies context-based attention to nodes, enhancing image retrieval performance. The key advantage of GCNs is their ability to encode neighbourhood information into each segment through message-passing operations, facilitating more context-aware feature extraction.

Patel et al. [Patel et al., 2023] propose a two-dimensional embedding approach to facilitate mass labelling. Their method first generates features using an Autoencoder (AE), followed by dimensionality reduction techniques such as t-SNE and UMAP. These techniques are useful for preserving local distances between data points when reducing dimensionality, which aids in visualising machine learning results [Ali et al., 2019, 2021]. In particular, they employ these embeddings to extract, visualise, and label features from images in a two-dimensional space, allowing for easy exploration via interactive tools like pan, zoom, and brushing. However, their approach struggles with certain outliers. For instance, in their study, the orientation and intensity of textural features caused clouds in satellite imagery to be incorrectly clustered with land and water borders, leading to inaccuracies in labelling.

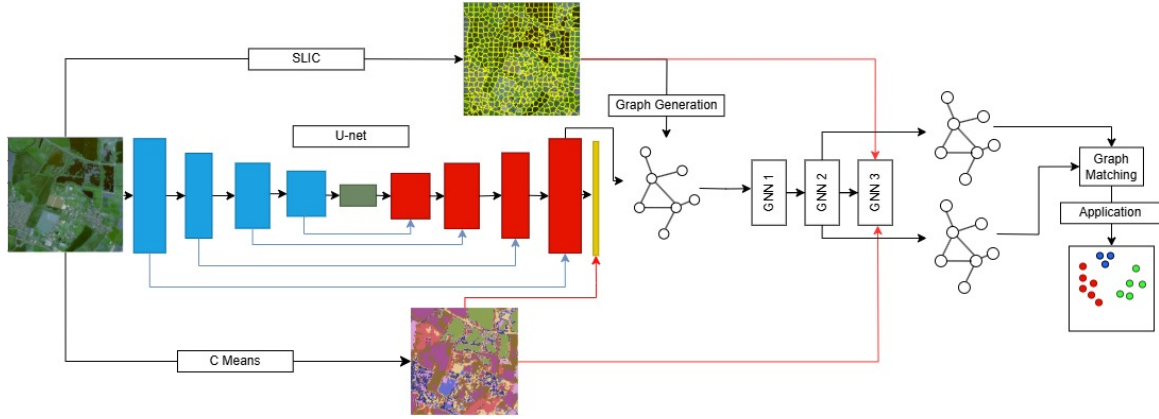


Figure 1: This diagram illustrates the data flow within the pipeline. Blue boxes represent the contracting layers of the U-Net, red boxes the expansive layers, and yellow the predictive layer. Blue lines indicate skip connections. Red lines show how data is used in the loss function, where the third GNN layer reshapes its input to enable comparison with the targets.

Patel et al.’s method is limited by issues of feature misalignment due to a lack of contextual understanding. In contrast, we aim to improve the robustness of feature embeddings by integrating **Graph Neural Networks (GNNs)** and **context-based attention mechanisms**, which encode neighbourhood relationships and enable the creation of more accurate, context-aware embeddings for satellite imagery. Our method mitigates the impact of outliers and provides a more reliable tool for visual labelling, ultimately enhancing both the quality and precision of dataset creation.

In this paper, we propose an enhanced unsupervised feature extraction method for visual labelling and exploration. Specifically, we make the following contributions:

- A) We improve the coherence of embedding spaces by achieving tighter cluster formation, facilitating easier navigation through unsupervised clustering.
- B) By integrating Graph Neural Networks (GNNs) and feature encoding on image segmentations, we demonstrate that the resulting two-dimensional embedding space is rotationally invariant, making the approach more robust to spatial transformations.
- C) Finally, we apply this methodology to develop an advanced interactive tool for exploration and labelling, enhancing both efficiency and accuracy in labelling tasks.

## 2 Materials and Methods

The proposed pipeline consists of three key components (Figure 1): a U-Net for feature extraction, a Graph Neural Network (GNN) for generating relational embeddings, and a graph-matching algorithm for assessing graph similarity. The U-Net, like most convolutional networks, learns a generalised representation of the input data. The goal is to enable the U-Net to process unseen images and produce activation maps that generalise well for downstream tasks. The next component in the pipeline is the GNN, which incorporates geographical context by capturing neighbourhood information. For example, it distinguishes between a water pixel surrounded by ocean versus one near a beach coastline. To convert the U-Net’s activation maps into a graph structure suitable for the GNN, segmentation (into super-pixels) is applied. Finally, graph-matching algorithms are used for dimensionality reduction and to quantify the similarity between graphs.

## 2.1 Dataset

We utilise the SWED dataset [Seale et al., 2022], compiled of Sentinel-2 images captured 2017–2021. The images are tiles, regions of 10,980m by 10,980m, taken in a single pass of the satellite. Minimal cloud coverage is present within the dataset, and each tile contains a diverse set of coastal landscape features from globally distributed locations.

## 2.2 Fuzzy C-Means target extraction

Due to the spatial resolution of most satellite platforms, pixel assignment can be ambiguous or uncertain [Zhang et al., 2024]. Fuzzy C-means extraction, unlike its K-means counterpart, assigns to each data point a degree of membership to each cluster. This likelihood per pixel for each class transforms the problem domain into a multi-label classification. We use all 12 channels for the training set and to reduce memory, we use subsampling during model training, where we sample every 56<sup>th</sup> pixel. Finally, we applied the clustering model to the entire image to attain a tile-wide classification. The resultant centroids do not necessarily relate to certain physical materials such as water or concrete, more so a representative of the most common pixel properties. The soft classification allows for generalisation of data that does not attribute fully to any centroid.

## 2.3 Pre-Processing

For processing by the U-Net and GNN we split the tile into chips. A chip is created by applying a sliding window of size 256 × 256 pixels to the larger image, with no overlap between consecutive windows. This results in 42 × 42 chips containing 10,752 × 10,752 of the original tiles 10,980 × 10,980 pixels. For training and testing, we split the dataset by taking every fourth chip in a top-down, row-by-row pattern for the test set obtaining a 75/25 split. The size of the chip is a balance between training size and preserving contextual neighbourhood information. The larger the image the more computationally expensive the resulting pipeline becomes however more information about neighbouring features can be encoded. Considering CNN filters, larger chips result in fewer edge cases.

## 2.4 CNN feature extraction

To learn the texture representation we utilise a CNN where the learning function considers the C-Means classification for an objective discrimination of features. The CNN of choice was a U-Net, with 5 layers each for the encoder and decoder. Starting with 64 kernels in the encoder, these are doubled for each consecutive layer to 1024 in the final layer and opposite for the decoder. The target of the model is the fuzzy C-Means predictions. We used 2, 8 and 18 clusters to explore the performance of the U-Net. As each fuzzy classification is non-exclusive, a multi-label loss function is used. The loss function combined Dice loss and binary cross entropy Seale et al. [2022].

$$d(i) = 2 \times \frac{\sum(X_i \cdot Y_i)}{\sum(X_i) + \sum(Y_i)}$$

$$D = \frac{1}{C} \sum_{i=1}^C d(i)$$

As each class has its respective probability we can calculate the loss for each class,  $d(i)$  and average,  $D$ . Here  $d(i)$  is the dice loss for one class  $i$ ,  $X_i$  is the true probability and  $Y_i$  is the predicted. Finally

$C$  is the number of classes. Similarly, we calculate binary cross-entropy loss concerning each class and average. The final loss combining the two is a variation of combo loss [Taghanaki et al., 2019].

The final convolutional layer of the CNN produces the same image shape as the input with 64 convolutional activation maps in contrast to the 12 spectral channels. To combat over-fitting we applied random rotation and noise to the training set to increase the variation artificially. In addition, we applied early stopping when the loss was no longer reducing after 15 epochs. There is an increase in loss as the number of fuzzy C-means classes increases as we discriminate between even finer spectral detail.

## 2.5 Graph Construction

Nodes for the graphs are determined by the Simple Linear Iterative Clustering (SLIC) algorithm [Achanta et al., 2012] where each segment is considered a new node. SLIC produces local homogeneous parcels which for encoding geographical neighbours is ideal. We set the target number of segmentations for SLIC as  $N = 500$ . The target number was chosen to over segment an image resulting in a roughly  $1310m^s$  coverage for each segment, compromising computational cost in order to encode smaller features. This is only a target as SLIC can vary  $N$  based on each sample as it splits or merges segments. The features of each node are  $F_i = \{\bar{A}\}$ . Where  $\bar{A}$  is the mean values of each of the 64 activation maps from the CNN for each segment. Edges for each segment are determined by the  $K$  geographically nearest segments. We tested on eight  $K$  nearest neighbours. This work differs to previous work by Diao et al. [Diao et al., 2022] because we only include information from the CNN and rely on geographical neighbours to construct edges. The resulting representation is a Graph  $G(V, E)$  with  $N = V$  number of nodes with 64 features  $F$  each. There are  $K \times N$  unweighted edge connections between nodes,  $\approx 8 \times 500$  edges.

## 2.6 Graph Neural Network

The graph attention network is 3 layers with attention mechanisms [Brody et al., 2021]. The final layer produces the  $C$  dimensional output for each class predicted. The loss function is categorical cross entropy for each predicted class compared to the averaged C-mean of each segment. The new hidden feature vector for each node,  $\mathbf{X}'_i$  can be calculated with the following:

$$\mathbf{X}'_i = \parallel_{k=1}^K \sigma \left( \sum_{j \in N(i) \cup i} \alpha_{ij} \mathbf{W}^k \mathbf{x}_j \right)$$

where  $k$  is the number of attention heads,  $\parallel$  denotes vector concatenation,  $\sigma(\cdot)$  is an activation function,  $N$  is the Neighbourhood of edges to  $i$ ,  $\mathbf{W}^k$  is a matrix of parameters for the  $k$ -th attention head and  $\alpha_{ij}$  are attention coefficients defined by the following:

$$\alpha_{ij} = \frac{\exp(\mathbf{a}^T \text{LeakyReLU}([\mathbf{W}\mathbf{x}_i \parallel \mathbf{W}\mathbf{x}_j \parallel \mathbf{e}_{ij}]))}{\sum_{k \in N(i) \cup i} \exp(\mathbf{a}^T \text{LeakyReLU}([\mathbf{W}\mathbf{x}_i \parallel \mathbf{W}\mathbf{h}_k \parallel \mathbf{e}_{ik}]))}$$

where  $\mathbf{e}_{ik}$  is an edge between node  $i$  and connected node  $k$ .

Each hidden feature vector for a node has 64 variables, given that our ultimate goal is to visualise and compare similarities we need to maintain or reduce the size of the feature vector in favour of improved computational performance over accuracy. This is achieved by reducing the output feature dimensions of the GAT layers. In our experiments, the extracted features are the output of the second

to last GAT layer, within this layer we constrict the output of the features to 8 hidden feature vectors with 8 attention heads. Therefore our final representation is a 64-dimensional vector. The third layer reshapes this vector to enable comparison with the targets in the loss function.

Similarly we tested a 3 layer graph convolutional network (GCN) with an embedding vector of 60 hidden features. The choice of testing both networks is to see if the inclusion of an attention mechanism impacts the information in each node in relation to its neighbours.

For these and the above parameters we systematically explored various parameter configurations (e.g., number of GNN edges, U-Net and GCN layers, nearest neighbourhood for SLIC) and selected those that provided the best trade-off between accuracy and computational efficiency, focusing on parameters that had the most significant impact on performance (see Sections 3.4 and 3.5).

## 2.7 Graph Matching

For each chip in our pipeline, we obtain a graph  $G(V, E)$  where each node  $V$  is linked by edge  $E$ . A node refers to a singular segmentation within the chip (see the yellow outlined segments in Figure 1). Edges are connections to the nearest neighbouring nodes in feature space,  $X$  from the second layer of the GNN. The second layer is chosen as it provides contextual information for each segment as it encodes neighbours from two hops away, neighbours of neighbours (this is evaluated in Section 2.9.2). Graph matching finds how similar two graphs are based on their node and edge composition. As our approach utilised many segments our resulting nodes are in the hundreds, therefore, utilising multi-graph solvers which take into account both vertices and edges is infeasible in both memory and computational complexity. We simplify the matching to a bi-partite graph representation using the Hungarian algorithm to match nodes present in both graphs and calculate the overall similarity based on the distance between matched nodes in feature space  $X$ . Applying the matching to create a similarity matrix for every chip processed through UMAP [McInnes et al., 2020] creates a two-dimensional embedding for visualisation as follows in Section 2.8.

## 2.8 2D Projections

We provide the user an interface that can switch between two modes. In the higher-level mode, users interact with  $256 \times 256$  pixel chips. In the lower-level mode, users interact with the segments. In both cases, the user interacts through a 2D UMAP projection of the manifold – Figure 2 (top) – and sees the relevant chips or segments in the view below – Figure 2 (bottom).

UMAP requires either a set of vectors representing each data point or a precomputed similarity matrix, typically based on pairwise distances or cosine similarities. Low-level segments are represented by a singular 64 or 60-dimensional vector from the graph attention networks and are readily available for UMAP projection. Higher-level chips are represented as graph structures, where each node corresponds to a 64 or 60-dimensional vector. To compare two chips, we apply Hungarian matching to align their nodes, producing a one-to-one correspondence between vectors. We then compute the cosine similarity for each matched pair and average these values to obtain an overall similarity score between the two chips. Repeating this process across all chip pairs yields a similarity matrix, which serves as input to UMAP for generating the high-level 2D projection.

## 2.9 Evaluation

To test the GNN part of our architecture, we define two levels of similarity evaluation between the SLIC super-pixels (segments) – feature-based and context-aware.

### 2.9.1 Graph Evaluation I: Feature-based

Under feature-based evaluation the SLIC segments are fed into each GNN, producing feature space,  $X$ . For each segment, we compare it to its closest segment within the feature space. The comparison was made using four common similarity measures; gray level occurrence matrix (GLCM), linear binary patterns (LBP), Structured similarity index measure (SSIM) and spectral angle mapper (SAM). The first two measures were calculated via a bounding box that enclosed the segment, the latter two purely on the content within the segment. This test allows us to find the conditions and parameters that produce the best GNN.

### 2.9.2 Graph Evaluation II: Context-aware

Under context-aware evaluation, we enhance the evaluation by considering spatial context. For each segment  $x$ , we evaluate its similarity not only to  $y$  in feature space but also by taking into account the 8 nearest spatial neighbours of both segments. The similarity between  $x$  and  $y$  is then adjusted to ensure that the spatial arrangement of their neighbours is also preserved. We use the Hungarian matching algorithm to find the optimal one-to-one correspondence between the neighbours of  $x$  and those of  $y$ , to test neighbourhood preservation. This context-aware evaluation leads to a more accurate representation of the similarity between super-pixels, reflecting both feature similarity and spatial proximity. The one-to-one correspondence resulting from the bi-partite matching, leads to 9 nodes pairs, each pair consisting of two segments, either  $x$  or a neighbour of  $x$  and  $y$  or a neighbour of  $y$ . Each pair's similarity is then computed with GLCM, LBP, SSIM and SAM and averaged for all nine pairs.

### 2.9.3 U-Net Evaluation

Part of our architecture is a U-Net that provides unsupervised features to feed into the GNN and graph matching. For this evaluation we compare our U-Net architecture to the state-of-the-art approaches of using ResNet-50 and GoogLeNet [Helber et al., 2019]. The benchmarked approaches [Helber et al., 2019] were pre-trained on millions of images and then fine-tuned on EuroSat data. We utilise our pre-trained U-Net with two additional linear layers appended for classification. Our U-Net being pre-trained on only 1411 images, from a singular geographical region. If this test achieves an accuracy close to state-of-the-art we can attest that our U-Net, with some fine-tuning, has learnt rich features for the remaining parts of our pipeline. Successful application of the U-Net on a larger and more geographical diverse dataset also would demonstrate geo-generalisable weights.

### 2.9.4 Tool Evaluation

Additional to the above approaches, we also provide an evaluation of our interactive application that allows the user to explore and label the final features produced in two dimensions via UMAP for exploration and labelling. **Please refer to the video submitted as a supplementary file** for an example exploration of the feature space to label at both the top chip level and the segmentation level. A public version is available at YouTube, and is archived at Zenodo Patel and Jones [2025].

## 3 Results

### 3.1 Remote Sensing Labelling Application (see 2.9.4 Tool Evaluation)

Our pipeline enables advanced interaction within our labelling tool. Referring to the **provided video** Patel and Jones [2025] of the tool utilised on the dataset, this section presents frames extracts from the video to demonstrate and discuss functionality.

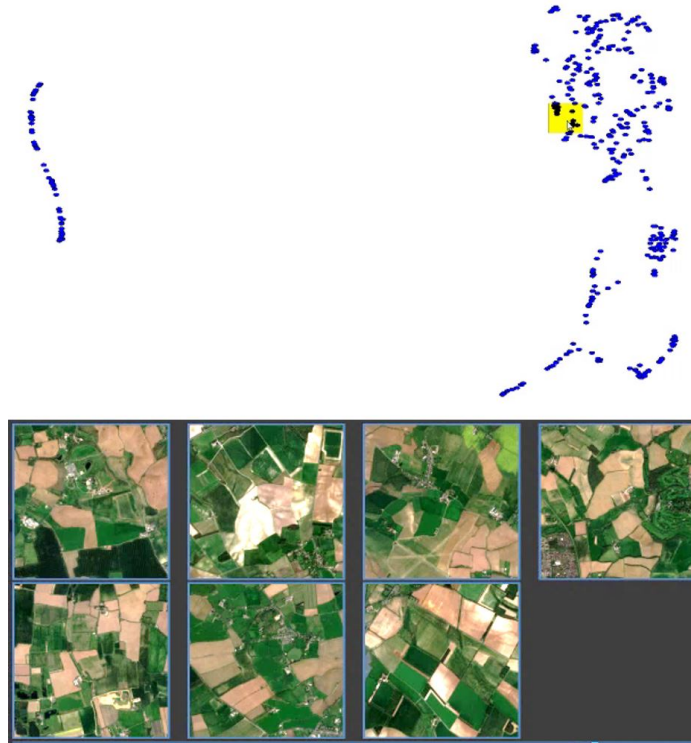


Figure 2: UMAP dimension reduction to 2D on the graph matching output of our entire pipeline. At this level, each point represents one chip. The user interactively highlights a resizable region which can be dragged across the manifold representation. Chip images represented by the 2D points within the highlight are displayed in the pane below. Training did not use any labelled data. (Video frame edited to save space in the paper).

The main contributions are (**Section 3.1.1**) the tool allows exploration of feature space,  $X$ , via a two-dimensional interface where our pipeline has resulted in successful organisation of the high dimensional manifold. The resultant clusters are compact and contain visually related images. (**Section 3.1.2**) embedded images with large texture gradients have no adverse impacts on the similarity measure using our approach. (**Section 3.1.3**) we significantly extend previous labelling approaches by enabling this interaction on pixel-based segmentations within the larger images, thus allowing fast labelling at a finer granularity.

### 3.1.1 Cluster exploration

In Figure 2 (top), the user interacts with the 2D manifold representation of the  $256 \times 256$  chip-level data by brushing selected points. The brushed points, highlighted in yellow, correspond to specific source images, which are simultaneously displayed in the image pane (Figure 2, bottom). This particular cluster reveals a patchwork of fields. The accompanying video illustrates the manifold’s spatial evolution by showing image chips transitioning through farmland, industrial zones, residential areas, increasing water bodies (e.g., lakes and sea), and other geographical features.

Figure 3 shows more example content of the embedding space. Samples drawn and shown from the clusters contain mainly sea (A), land with water (B), dense built-up areas (C) and farmland (D). Area A in the embedding is consistently majority water content, there is very little presence of land. However, the features within that cluster do not differentiate between any features such as boats or

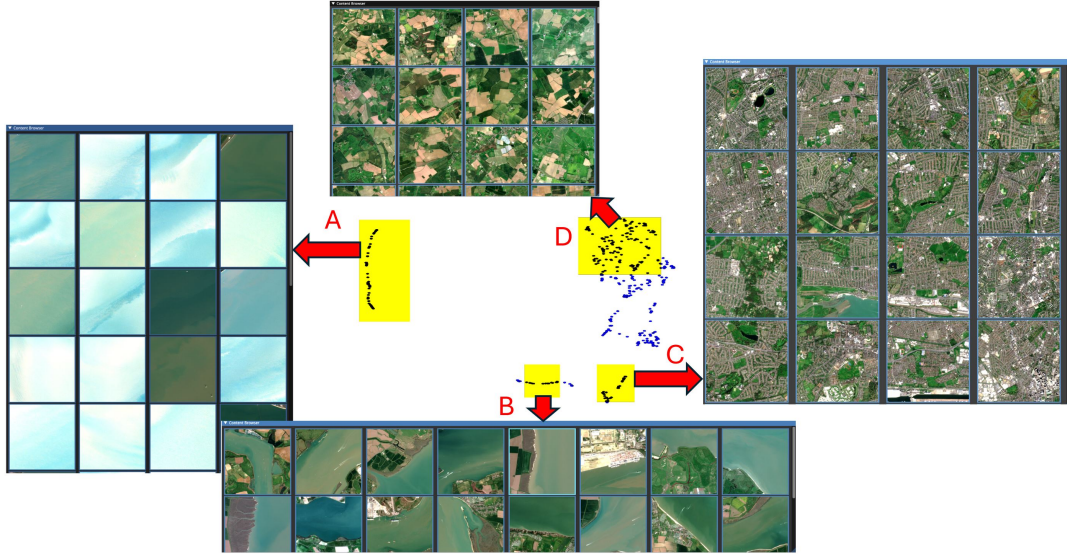


Figure 3: Example of the U-map embedding dimensionality reduction of high dimensional feature space,  $X$ , output from the final graph matching stage of our entire pipeline. Training was unsupervised. The images selected by the user highlights are shown in the display pane with the labels A-D explained in Section 3.1.1.

offshore installations. Sample space B includes nearly all water content features present near land, the cluster sits directly between A and D which are exclusively just land or water. This evolution of features shows at the chip level that water content is a highly relevant feature for similarity.

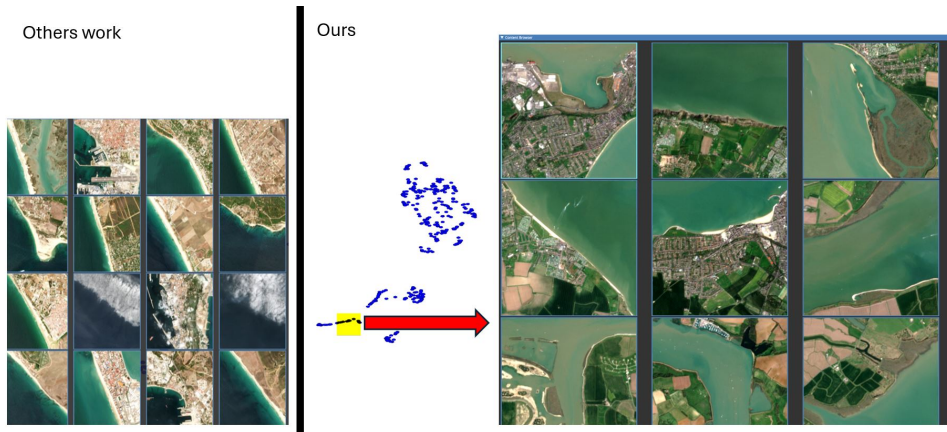


Figure 4: Example of the UMAP embedding space from [Patel et al., 2023], showing results influenced by strong texture similarities due to edge alignment, and a comparison with our approach, which introduces rotational invariance to remove this strong alignment.

### 3.1.2 Rotational Invariance (Figure 4)

Within our application, the utility of representing our images as segmentations with mean feature aggregation has a two-fold effect. Firstly, rotational invariance is introduced by Hungarian matching disregarding the geographical layout of features, as only segments are compared. Secondly, taking

the mean of each feature map removes any encoding of strong gradient changes within the activation maps. For an example of both, we refer to Figure 4. Work produced by [Patel et al., 2023] shows an example of a large textural and spectral disparity between land and sea. The clustering has been directly influenced by the orientation of this boundary, with the inclusion of outliers containing cloud and water where they follow the same gradient. In comparison our work has ignored strong directional gradients within the image data, e.g. see Figure 3. In Figure 4, we visually selected a cluster also of approximately 50/50 land/water coverage, which indicates there is no obvious common directional gradient.

### 3.1.3 Segmentation Analysis (Figure 5)

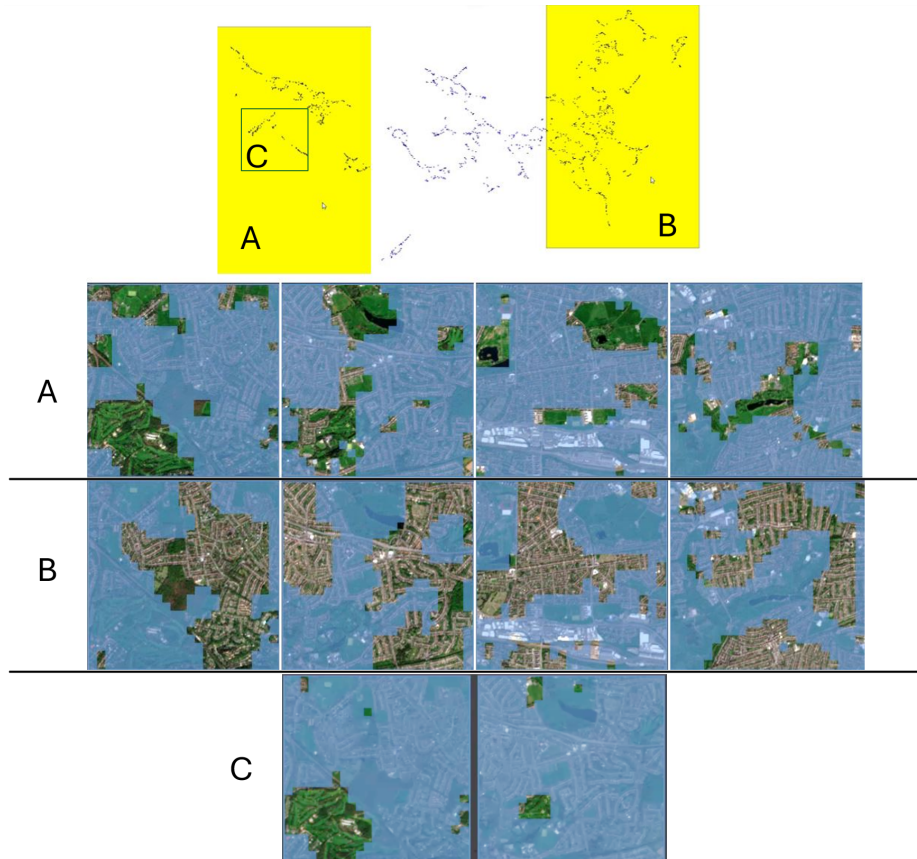


Figure 5: Example (from video) of projecting four images and exploring their segmentations to label as urban or vegetation. The left selection, (A), shows the largely vegetation segments in the first row of images and (B) largely urban development in the same four images, but demonstrated in the second row. (C) is a selection in the manifold of segmentations which related to golf courses and are present on different images as displayed on the third row (the golf course example is in the video).

A major contribution is enabling finer sub-image labelling based on the segmentations. The user starts by selecting images they wish to examine in detail. A new interactive 2D projection of the feature space,  $X$ , is displayed where each point represents a single (SLIC) segmentation within the images. Similar to the image exploration, our approach produces a successful organisation of the manifold where segments are very closely related. In Figure 5 we see at the top the 2D interactive display where each point represents one segment within the image data. By brushing multiple points in 2D, the user will see all corresponding segmentations in the reference images below. This manifold

evolves from vegetation on the left to largely urban areas on the right. Here we combine two frames from the video where the left selection displays the vegetation with some urban features (top row of images), and the right selection displays the almost pure urban features (bottom row of images). This empowers the expert to quickly label at a fine level of segmentation (as demonstrated in the video).

The third row shows a further example of extracting features that share common geographical neighbourhoods, in this particular example golf courses. Although unsupervised, the embedding space has clustered larger and smaller golf courses irrespective of their sizes. The video demonstrates an example of how to build up a labelling of the golf course data through selection and filtering data points in the manifold.

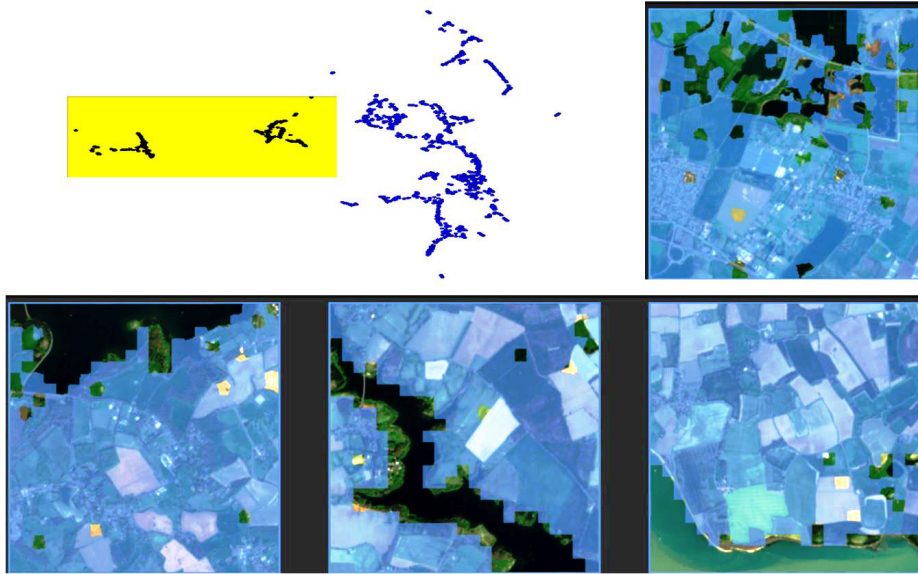


Figure 6: Example of extracting water features at segment level. There are various water features including lakes, rivers and sea. Here, as in Figure 5, the semi-transparent blue indicates the areas masked away, and the full colour segments (which are dark because they are water features) are the selected areas for labelling.

The projection at segment level has also clustered the various water bodies within the images (figure 6). Via exploring the manifold, the user is able to make a selection that segments water features effectively. We found that various different forms and sizes of water bodies including large bodies of water are easily selected via the interface and extracted simultaneously.

### 3.2 U-Net Test (proposed in U-Net Evaluation 2.9.3)

The aim of this test is to evaluate whether the U-Net part of our architecture achieves close to state-of-the-art performance to feed into the rest of our graph neural networks, graph matching and interactive application pipeline.

In order to validate the utility and generalisable application of the methodology we want to demonstrate that the trained U-Net (trained using unsupervised C-means clustering) is generalisable. In order to evaluate the U-Net we compare to a benchmark experiment on the EuroSat dataset [Helber et al., 2019]. The dataset consists of 27,000 labelled images from Sentinel-2 mission covering ten separate classes. We resized the images from 64x64 to 256x256 to match the training data. We did

Method	Accuracy
EuroSat ResNet-50	98.57
EuroSat GoogleLeNet	98.18
C=2 linear layers	93.24
C=8 linear layers	97.43
C=18 linear layers	93.42

Table 1: Respective classification accuracies for each model tested where C is the initial C means clustering number. Results labelled EuroSat where taken from [Helber et al., 2019].

not apply bottom-of-atmosphere correction. The Eurosat models were pre-trained on 1.2 million images from the ILSVRC-2012 dataset.

We append and train two additional linear layers for class prediction on the EuroSAT dataset. Our aim is to evaluate if the learnt weights are generalisable and whether the model can find an appropriate minimum given a starting feature space. Despite not using a traditional classification model (we use a U-Net) and pre-training on a much smaller dataset, our approach achieves performance comparable to state-of-the-art methods (Table 1). This validates the U-Net component of our architecture.

### 3.3 Graph Encoding Comparison (see 2.9.1 Graph Evaluation)

We trained GCN and GAT variations of graph networks against C-means clusters with C=2, 8 and 18. These were evaluated using various similarity measures. GLCM and LBP indicate the textural differences between images. SSIM measures structure, contrast and luminance. SAM is based solely on the mean spectral difference between each segment. This section analyses the construction of our embedding spaces by determining the effect of the different C-means cluster number on the pipeline.

Model	GLCM↓	LBP↑	SSIM↑	SAM↓
GCN 2	16.2770	0.8571	0.9120	0.3321
GCN 8	<b>15.4685</b>	<b>0.8716</b>	<b>0.9287</b>	<b>0.2887</b>
GCN 18	15.5322	0.8671	0.9243	0.3017
GAT 2	16.0025	0.8633	0.9201	0.3112
GAT 8	15.5676	0.8704	0.9256	0.2942
GAT 18	15.7663	0.8673	0.9237	0.2992

Table 2: Average of each similarity measure over every pair of nearest neighbouring segments in feature space,  $X$ , created by each method. This corresponds to Section 2.9.1 Feature-based graph evaluation.

This first experiment computes the measures between each segment, A, and its nearest neighbour, B, in the feature space  $X$  (Table 2) and average that over all the segments. This tests whether the GNN places similar segments together in the feature space. The number of C-means clusters exhibits low sensitivity, and we therefore fix C=8 as the optimal choice for our model.

The second experiment will find the eight spatially closest segmented neighbours in the original image to A. It also finds the eight spatially closest segment neighbours to B. Hungarian matching is then used to pair segments between these two neighbourhoods, forming nine matched pairs.

Model	GLCM↓	LBP↑	SSIM↑	SAM↓
GCN 2	14.4610	0.8983	0.9589	0.2152
GCN 8	<b>13.7904</b>	<b>0.9034</b>	<b>0.9624</b>	<b>0.2064</b>
GCN 18	13.7278	0.9033	0.9620	0.2066
GAT 2	14.2259	0.9000	0.9560	0.2122
GAT 8	14.0145	0.9018	0.9613	0.2092
GAT 18	14.0557	0.9013	0.9611	0.2100

Table 3: Average of each similarity measure over every pair of nearest neighbouring segments. The similarity between each segment takes into account the context of its local geographical neighbourhood as described in the referring text. This corresponds to Section 2.9.2 Context-aware graph evaluation.

The similarity measures are computed for each pair to assess how similar the neighbourhoods are. This experiment tests whether segments with similar local contexts, implicitly captured by the two graph layers, are also close in the learned feature space. Ideally, the feature space should position segments near others that share similar neighbourhood structures. For example, a small body of water surrounded by urban segments should be placed near other similarly situated water bodies.

Overall the aim of this test is to evaluate that our pipeline is able to place segments of a certain type and surrounding close within the feature space as this lends itself to being the best interaction for a user by enforcing local structural awareness. The best similarity results were for eight clusters and GCN type was better than GAT, see Table 3. From our results presented in the video it is possible to see that segments are contextually close making the labelling easier. The graph convolutional network, trained on eight C-means clusters seems to be the best balance in our tests and was therefore used in our pipeline, although again there is low sensitivity to cluster number. Overall these models take into account the neighbourhood and texture more than the individual segments or spectral differences.

### 3.4 Parameter Sensitivity

In this section we explore the parameter sensitivity for two key values within the pipeline. These two parameters are the initial  $K$  value and  $N$  for SLIC during the graph construction phase, Section 2.5. The variations in parameters are tested via our context-aware approach to segmentation comparison detailed in Section 2.9.2. We also report results when utilising only the CNN output and the first layer of the GCN. These tests are compared against the best pipeline (GCN 8) where  $K = 8$  and  $N = 500$  segments in the SLIC algorithm.

K	GLCM↓	LBP↑	SSIM↑	SAM↓
4	14.2846	0.8992	0.9583	0.2140
8	13.7904	0.9034	0.9624	0.2064
12	<b>13.2240</b>	<b>0.9075</b>	<b>0.9649</b>	<b>0.1988</b>

Table 4: Comparison of varying  $K$ , during the graph construction phase (Section 2.5).

We used 8 edges during the graph generation phase. Here we compare results for  $K \in \{4, 8, 12\}$ . Our pipeline shows an improvement in for larger number of edges ( $K$ ) in the neighbourhood (Table 4). Increasing the number of edges ( $K$ ) increases the GCN training time and graph matching. For example, given the Hungarian algorithm’s complexity of  $O(N^3)$ , where  $N$  is the sum of all nodes in both graphs, the complexity for  $K = 8$  is  $16^3$  whilst  $K = 12$  is  $24^3$ . Correspondingly, for the GCN training times for  $K = 8$  was 1.6 hours and  $K = 12$  was 6.6 hours. In our tests, larger  $K$  produces more accuracy, but at significantly slower training times, and therefore we used  $K = 8$  as a good balance.

SLIC	GLCM↓	LBP↑	SSIM↑	SAM↓
200	<b>12.4336</b>	0.8888	0.9166	0.3608
500	13.7904	<b>0.9034</b>	<b>0.9624</b>	<b>0.2064</b>
800	14.8003	0.8604	0.9404	0.2819

Table 5: Comparison of varying SLIC parameter  $N$ , used during the graph construction phase Section 2.5.

Here we report values of  $N \in 200, 500, 800$  for the number of SLIC segments. Our initial choice,  $N = 500$ , was to cover an approximate area of  $1300m^2$  for ease of interpretability and efficiency when visualised for the user (the mean average size of segments is  $256 \times 256 \div 500 = 131$  — approximately 11 by 11 pixels and each pixel is  $10m^2$  in Sentinel-2). A smaller area allows finer labelling at the cost of speed, namely projecting and labelling more points. This choice for  $N$  was also optimal when considering local neighbourhood encoding using the different measures, see Table 5. For smaller  $N$  values, we see that comparing segments via GLCM shows better results however, over all measures  $N = 500$  is the most accurate.

### 3.5 Graph layer ablation

Image Representation	GLCM↓	LBP↑	SSIM↑	SAM↓
Graph Generation	14.6613	0.8970	<b>0.9853</b>	0.2165
Layer 1	14.3951	0.8988	0.9590	0.2147
GCN Layer 2	<b>13.7904</b>	<b>0.9034</b>	0.9624	<b>0.2064</b>

Table 6: Comparison of utilising different outputs for the final graph representation, the graph construction phase Section 2.5 and the first layer of the GCN. These are compared to the ideal pipeline, GCN with 8 C-means.

Finally, we validate our architecture by conducting an ablation study on the use of embeddings from our graph output. Our architecture produces graph outputs at three stages: (1) during graph generation, which combines the CNN U-Net output and SLIC; (2) at the output of GCN layer 1; and (3) at the output of GCN layer 2, which is the version reported throughout this work. The output of GCN layer 3 is a learnt reshaping from the second layer, from hidden dimension to C-means predictions, used only for the loss function. As such, it is not suitable for use as an embedding.

Table 6 demonstrates that selecting GCN layer 2 as the embedding layer yields optimal performance on three of the metrics related to texture and spectral similarity, which are particularly relevant to our

interactive pipeline. The only exception is SSIM, where the combination of CNN U-Net output and SLIC performs best.

## 4 Discussion

Our pipeline creates a 2D interactive interface that enables users to apply labels to segments and chips extracted from remote sensing (RS) images. We demonstrate that unlabelled data can be effectively leveraged using C-means clustering, SLIC segmentation, and a U-Net architecture, all of which contribute to the loss function of a graph convolutional network (GCN). The GCN takes as input the SLIC segments and the final layer of the U-Net, allowing it to learn representations that capture both individual segment features and their spatial context. The resulting graph embeddings are compared using Hungarian matching to assess neighbourhood similarity. These comparisons are used to construct a similarity matrix, which is then projected into 2D using UMAP to power the interactive interface.

By exploring hyperparameters, we arrive at an optimal model and architecture that, as shown in the accompanying video, enables intuitive and efficient interaction with both high-level chips and low-level segments. We validated key components of the model and provided a quantitative assessment of its performance including sensitivity and ablation study.

The high ingestion rate of remote sensing (RS) data and the need for labelled datasets remain major challenges – especially in emerging or niche application areas where accurate, up-to-date labels are scarce. Creating large, high-quality datasets typically requires costly expert input. To address this, our proposed application framework reduces labelling effort by enabling users to find similar features across RS images. Presenting data as image chips, rather than traditional map views, streamlines the labelling of large areas. While map-based projections offer geographic context, chips allow users to more easily assess visual and contextual similarities. Future work could integrate both views through a coordinated interface.

Remote sensing (RS) data captures the physical properties of surface materials, which reflect light at varying intensities depending on the recorded wavelength. Within a single  $10m^2$  pixel, multiple materials may contribute to the signal, resulting in mixed spectral responses, therefore, spectral unmixing was the original inspiration behind our generalisable CNN model. Our use of fuzzy clustering emulates this principle by allowing soft associations between segments and composite material types. However, an open question remains: could the pipeline be further improved by integrating spectral unmixing algorithms Feng et al. [2022] commonly used in the RS community? Alternatively, incorporating a priori knowledge of material reflectance properties could guide centroid selection to better target or generalise the labelling process.

The graph matching process within this pipeline and the tests poses an interesting computational problem. Whilst Hungarian matching can be processed on graphics cards reducing time taken it still remains a costly problem to solve. The complexity is  $O(n^3)$  where  $n$  is the count of nodes in both graphs. In order to save time this process could be estimated via an AI model. Similarly UMAP and t-SNE could be solved by training parametric models Sainburg et al. [2021], Svantesson et al. [2023]. Large dataset projections could be calculated offline to user interaction however branched projections of many segments could benefit greatly from parametric models.

At the low-level we allow users to label segments. Even lower pixel-level classification would require future work to improve the segmentations where only extremely similar or identical pixels are grouped. This could impact the time complexity of the graph matching as more segmentations would be required also placing more demand on dimensionality reduction. Alternatively segments could be

organised hierarchically and presented to a user for accurate pixel level classification, therefore only computing relevant information when needed.

## Acknowledgements

This research was funded by EPSRC grant number EP/S021892/1 and UKHO. For the purpose of open access the authors have applied a Creative Commons Attribution (CC BY) license to any Author Accepted Manuscript version arising from this submission.

## Declaration of Interest Statement

The authors declare that they have no known competing financial interests or personal relationships that could have appeared to influence the work reported in this paper.

## References

- R. Achanta, A. Shaji, K. Smith, A. Lucchi, P. Fua, and S. Süsstrunk. SLIC superpixels compared to state-of-the-art superpixel methods. *IEEE Transactions on Pattern Analysis and Machine Intelligence*, 34(11):2274–2282, 2012. doi:10.1109/TPAMI.2012.120.
- H. Ahmadi and E. Pekkan. Fault-based geological lineaments extraction using remote sensing and GIS—a review. *Geosciences*, 11(5):183, 2021. doi:10.3390/geosciences11050183.
- M. Ali, M. W. Jones, X. Xie, and M. Williams. Timecluster: Dimension reduction applied to temporal data for visual analytics. *The Visual Computer*, 35(6):1013–1026, 6 2019. ISSN 1432-2315. doi:10.1007/s00371-019-01673-y.
- M. Ali, R. Borgo, and M. W. Jones. Concurrent time-series selections using deep learning and dimension reduction. *Knowledge-Based Systems*, 233:107507, 12 2021. doi:10.1016/j.knosys.2021.107507.
- P. Bosilj, E. Aptoula, S. Lefèvre, and E. Kijak. Retrieval of remote sensing images with pattern spectra descriptors. *ISPRS International Journal of Geo-Information*, 5(12):228, 2016. doi:10.3390/ijgi5120228.
- S. Brody, U. Alon, and E. Yahav. How attentive are graph attention networks? *arXiv preprint arXiv:2105.14491*, 2021. doi:10.48550/arXiv.2105.14491.
- Y. Cao, C. Wang, Z. Li, L. Zhang, and L. Zhang. Spatial-bag-of-features. In *2010 IEEE Computer Society Conference on Computer Vision and Pattern Recognition*, pages 3352–3359. IEEE, 2010. doi:10.1109/CVPR.2010.5540021.
- B. Chaudhuri, B. Demir, S. Chaudhuri, and L. Bruzzone. Multilabel remote sensing image retrieval using a semisupervised graph-theoretic method. *IEEE Transactions on Geoscience and Remote Sensing*, 56(2):1144–1158, 2018. doi:10.1109/TGRS.2017.2760909.
- U. Chaudhuri, B. Banerjee, A. Bhattacharya, and M. Datcu. Attention-driven graph convolution network for remote sensing image retrieval. *IEEE Geoscience and Remote Sensing Letters*, 19: 1–5, 2022. doi:10.1109/LGRS.2021.3105448.
- S. Chen, S. Zhong, B. Xue, X. Li, L. Zhao, and C.-I. Chang. Iterative scale-invariant feature transform for remote sensing image registration. *IEEE Transactions on Geoscience and Remote Sensing*, 59(4):3244–3265, 2020. URL 10.1109/TGRS.2020.3008609.

- Q. Diao, Y. Dai, C. Zhang, Y. Wu, X. Feng, and F. Pan. Superpixel-based attention graph neural network for semantic segmentation in aerial images. *Remote Sensing*, 14(2), 2022. ISSN 2072-4292. doi:10.3390/rs14020305.
- A. Draganov and S. Dohn. Relating tSNE and UMAP to classical dimensionality reduction. *arXiv preprint arXiv:2306.11898*, 2023. doi:10.48550/arXiv.2306.11898.
- X.-R. Feng, H.-C. Li, R. Wang, Q. Du, X. Jia, and A. Plaza. Hyperspectral unmixing based on nonnegative matrix factorization: A comprehensive review. *IEEE Journal of Selected Topics in Applied Earth Observations and Remote Sensing*, 15:4414–4436, 2022. doi:10.1109/JSTARS.2022.3175257.
- A. Halladin-Dąbrowska, A. Kania, and D. Kopeć. The t-SNE algorithm as a tool to improve the quality of reference data used in accurate mapping of heterogeneous non-forest vegetation. *Remote Sensing*, 12(1):39, 2019. doi:10.3390/rs12010039.
- P. Helber, B. Bischke, A. Dengel, and D. Borth. Eurosat: A novel dataset and deep learning benchmark for land use and land cover classification. *IEEE Journal of Selected Topics in Applied Earth Observations and Remote Sensing*, 12(7), July 2019. doi:10.1109/JSTARS.2019.2918242.
- D. Hou, Z. Miao, H. Xing, and H. Wu. V-RSIR: An open access web-based image annotation tool for remote sensing image retrieval. *IEEE Access*, 7:83852–83862, 2019. doi:10.1109/ACCESS.2019.2924933.
- L. Huang, C. Chen, W. Li, and Q. Du. Remote sensing image scene classification using multi-scale completed local binary patterns and fisher vectors. *Remote Sensing*, 8(6):483, 2016. doi:10.3390/rs8060483.
- X. Huang, X. Liu, and L. Zhang. A multichannel gray level co-occurrence matrix for multi/hyperspectral image texture representation. *Remote Sensing*, 6(9):8424–8445, 2014. doi:10.3390/rs6098424.
- R. Imbriaco, C. Sebastian, E. Bondarev, and P. H. N. de With. Aggregated deep local features for remote sensing image retrieval. *Remote Sensing*, 11(5), 2019. ISSN 2072-4292. doi:10.3390/rs11050493.
- H. Jégou, M. Douze, C. Schmid, and P. Pérez. Aggregating local descriptors into a compact image representation. In *2010 IEEE Computer Society Conference on Computer Vision and Pattern Recognition*, pages 3304–3311. IEEE, 2010. doi:10.1109/CVPR.2010.5540039.
- J. Kang, R. Fernandez-Beltran, D. Hong, J. Chanussot, and A. Plaza. Graph relation network: Modeling relations between scenes for multilabel remote-sensing image classification and retrieval. *IEEE Transactions on Geoscience and Remote Sensing*, 59(5):4355–4369, 2021. doi:10.1109/TGRS.2020.3016020.
- L. Karthikeyan, I. Chawla, and A. K. Mishra. A review of remote sensing applications in agriculture for food security: Crop growth and yield, irrigation, and crop losses. *Journal of Hydrology*, 586: 124905, 2020. doi:10.1016/j.jhydrol.2020.124905.
- J. Li, L. Meng, B. Yang, C. Tao, L. Li, and W. Zhang. LabelRS: An automated toolbox to make deep learning samples from remote sensing images. *Remote Sensing*, 13(11):2064, 2021a. doi:10.3390/rs13112064.
- Y. Li, J. Ma, and Y. Zhang. Image retrieval from remote sensing big data: A survey. *Information Fusion*, 67:94–115, 2021b. ISSN 1566-2535. doi:10.1016/j.inffus.2020.10.008.
- L. McInnes, J. Healy, and J. Melville. UMAP: Uniform manifold approximation and projection for dimension reduction. *arXiv preprint arXiv:1802.03426*, 2020. doi:10.48550/arXiv.1802.03426.

- P. Napoletano. Visual descriptors for content-based retrieval of remote-sensing images. *International journal of remote sensing*, 39(5):1343–1376, 2018. doi:10.1080/01431161.2017.1399472.
- T. Patel and M. W. Jones. Video supplement to: “Leveraging convolutional and graph networks for an unsupervised remote sensing labelling tool”, Aug. 2025. URL <https://doi.org/10.5281/zenodo.16676591>. Video supplement.
- T. Patel, M. W. Jones, and T. Redfern. Manifold explorer: Satellite image labelling and clustering tool with using deep convolutional autoencoders. *Algorithms*, 16(10):469, 10 2023. ISSN 1999-4893. doi:10.3390/a16100469.
- X. Qi, P. Zhu, Y. Wang, L. Zhang, J. Peng, M. Wu, J. Chen, X. Zhao, N. Zang, and P. T. Mathiopoulos. MLRSNet: A multi-label high spatial resolution remote sensing dataset for semantic scene understanding. *ISPRS Journal of Photogrammetry and Remote Sensing*, 169:337–350, 2020. doi:10.1016/j.isprsjprs.2020.09.020.
- T. Ranchin and L. Wald. The wavelet transform for the analysis of remotely sensed images. *International Journal of Remote Sensing*, 14(3):615–619, 1993. doi:10.1080/01431169308904362.
- A. Romero, C. Gatta, and G. Camps-Valls. Unsupervised deep feature extraction for remote sensing image classification. *IEEE Transactions on Geoscience and Remote Sensing*, 54(3):1349–1362, 2015. doi:10.1109/TGRS.2015.2478379.
- T. Sainburg, L. McInnes, and T. Q. Gentner. Parametric umap embeddings for representation and semisupervised learning. *Neural Computation*, 33(11):2881–2907, 2021.
- C. Seale, T. Redfern, P. Chatfield, C. Luo, and K. Dempsey. Coastline detection in satellite imagery: A deep learning approach on new benchmark data. *Remote Sensing of Environment*, 278:113044, 2022. ISSN 0034-4257. doi:10.1016/j.rse.2022.113044.
- J. Sivic and A. Zisserman. Video Google: A Text Retrieval Approach to Object Matching in Videos . In *IEEE International Conference on Computer Vision*, volume 3, page 1470, Los Alamitos, CA, USA, Oct. 2003. IEEE Computer Society. doi:10.1109/ICCV.2003.1238663.
- J. Song, S. Gao, Y. Zhu, and C. Ma. A survey of remote sensing image classification based on CNNs. *Big earth data*, 3(3):232–254, 2019. doi:10.1080/20964471.2019.1657720.
- G. Sumbul and B. Demir. A novel graph-theoretic deep representation learning method for multi-label remote sensing image retrieval. In *2021 IEEE International Geoscience and Remote Sensing Symposium IGARSS*, pages 266–269. IEEE, 2021. doi:10.1109/IGARSS47720.2021.9554466.
- Q. Sun and S. Bourennane. Hyperspectral image classification with unsupervised feature extraction. *Remote Sensing Letters*, 11(5):475–484, 2020. doi:10.1080/2150704X.2020.1731769.
- M. Svantesson, H. Olausson, A. Eklund, and M. Thordstein. Get a new perspective on eeg: convolutional neural network encoders for parametric t-sne. *Brain Sciences*, 13(3):453, 2023.
- S. A. Taghanaki, Y. Zheng, S. K. Zhou, B. Georgescu, P. Sharma, D. Xu, D. Comaniciu, and G. Hamarneh. Combo loss: Handling input and output imbalance in multi-organ segmentation. *Computerized Medical Imaging and Graphics*, 75:24–33, 2019. doi:10.1016/j.compmedimag.2019.04.005.
- X. Tang, X. Zhang, F. Liu, and L. Jiao. Unsupervised deep feature learning for remote sensing image retrieval. *Remote Sensing*, 10(8), 2018. ISSN 2072-4292. doi:10.3390/rs10081243.
- G. Wang, B. Fan, S. Xiang, and C. Pan. Aggregating rich hierarchical features for scene classification in remote sensing imagery. *IEEE Journal of Selected Topics in Applied Earth Observations and Remote Sensing*, 10(9):4104–4115, 2017. doi:10.1109/JSTARS.2017.2705419.

- Y. Wang, J. Song, K. Zhou, and Y. Liu. Unsupervised deep hashing with node representation for image retrieval. *Pattern Recognition*, 112:107785, 2021. ISSN 0031-3203. doi:10.1016/j.patcog.2020.107785.
- M. Weiss, F. Jacob, and G. Duveiller. Remote sensing for agricultural applications: A meta-review. *Remote sensing of environment*, 236:111402, 2020. doi:10.1016/j.rse.2019.111402.
- Y. Yan, H. Hao, B. Xu, J. Zhao, and F. Shen. Image clustering via deep embedded dimensionality reduction and probability-based triplet loss. *IEEE Transactions on Image Processing*, 29:5652–5661, 2020. doi:10.1109/TIP.2020.2984360.
- Y. Yang and S. Newsam. Comparing SIFT descriptors and gabor texture features for classification of remote sensed imagery. In *2008 15th IEEE international conference on image processing*, pages 1852–1855. IEEE, 2008. doi:10.1109/ICIP.2008.4712139.
- H. Yu, F. Yao, W. Lu, N. Liu, P. Li, H. You, and X. Sun. Text-image matching for cross-modal remote sensing image retrieval via graph neural network. *IEEE Journal of Selected Topics in Applied Earth Observations and Remote Sensing*, pages 812–824, 2022. doi:10.1109/JSTARS.2022.3231851.
- L. Zhang and L. Zhang. Artificial intelligence for remote sensing data analysis: A review of challenges and opportunities. *IEEE Geoscience and Remote Sensing Magazine*, 10(2):270–294, 2022. doi:10.1109/MGRS.2022.3145854.
- M. Zhang, Q. Cheng, F. Luo, and L. Ye. A triplet nonlocal neural network with dual-anchor triplet loss for high-resolution remote sensing image retrieval. *IEEE Journal of Selected Topics in Applied Earth Observations and Remote Sensing*, 14:2711–2723, 2021. doi:10.1109/JSTARS.2021.3058691.
- Y. Zhang, S. Yan, L. Zhang, and B. Du. Fast projected fuzzy clustering with anchor guidance for multimodal remote sensing imagery. *IEEE Transactions on Image Processing*, 33, 2024. doi:10.1109/TIP.2024.3444323.
- Q. Zhu, Y. Zhong, B. Zhao, G.-S. Xia, and L. Zhang. Bag-of-visual-words scene classifier with local and global features for high spatial resolution remote sensing imagery. *IEEE Geoscience and Remote Sensing Letters*, 13(6):747–751, 2016. doi:10.1109/LGRS.2015.2513443.